PSFC/JA-09-14

Localized measurement of short wavelength plasma fluctuations with the DIII-D phase contrast imaging diagnostic

J. R. Dorris, J. C. Rost, and M. Porkolab

October 2009

Plasma Science and Fusion Center
Massachusetts Institute of Technology
Cambridge MA 02139 USA

Localized Measurement of Short Wavelength Plasma Fluctuations with the DIII-D Phase Contrast Imaging Diagnostic

J. R. Dorris,* J. C. Rost, and M. Porkolab

Plasma Science and Fusion Center, Massachusetts Institute of Technology, Cambridge, Massachusetts 02139

(Dated: January 5, 2009)

A novel rotating mask system has been designed and implemented on the DIII–D Phase Contrast Imaging diagnostic to produce the first spatially localized PCI measurements of a tokamak plasma. The localization technique makes use of the variation of the magnetic field component perpendicular to the viewing chord as a function of chord height. This new capability provides measurements in the range $2 < k < 30$ cm^{-1}, 10 kHz $< f < 10$ MHz, $0.7 < r/a < 1$. This technique provides a spatial resolution of 10 cm at $k = 15$ cm^{-1} and can realistically provide measurements at a rate of 10 profiles/second. Calibration measurements show accurate characterization of the system transfer function making feasible a time dependent analysis that results in improved localization. Initial measurements show turbulence to peak near the plasma edge. This upgrade is part of a broader program to operate the DIII–D PCI at wavenumbers up to 40 cm^{-1} to probe electron scale turbulence in the plasma core.

PACS numbers: 52.35.Ra, 52.55.Fa, 52.70.-m

I. INTRODUCTION

Universally, tokamak experiments show particle and energy transport that is large compared to that predicted by collisional theories. This so-called anomalous transport is generally thought to arise from turbulent processes generated by microinstabilities [1]. Understanding the fundamental physics that govern these instabilities is a major focus of the international fusion community. These instabilities include drift-wave turbulence, the Ion Temperature Gradient (ITG) mode ($k_\perp \rho_{si} \sim 0.1$), the Trapped Electron Mode (TEM) ($k_\perp \rho_{si} \lesssim 1$), and the Electron Temperature Gradient (ETG) mode ($k_\perp \rho_{si} > 1$). Here $k_\perp$ is the component of the fluctuating wavevector perpendicular to the local magnetic field, $\rho_{si} = c_s/\omega_{ci}$ is the ion sound gyro-radius and c_s is the plasma sound speed. Simulations and measurements of long wavelength (ITG/TEM) turbulence generally agree that these modes drive ion thermal and particle transport [2, 3]. However, there is still controversy over the importance of short wavelength (ETG) modes [4]. Some simulations of short wavelength turbulence show substantial electron thermal transport due to ETG modes while other simulations show essentially none. The simulations differ in computational technique (*e.g.* fluid vs. particle in cell) as well as physics effects included (*e.g.* adiabatic ions vs. kinetic ions) [5]. These electron scale simulations are computationally expensive and are in various stages of maturity; however, none have been rigorously compared to experimental measurements. Confinement losses through the electron channel will be especially important in reactor-relevant plasmas due to strong thermal coupling between electrons and ions, and because fusion energy will be transferred from fast alpha parti-

cles to electrons. Understanding and subsequently controlling electron transport is therefore a major thrust in tokamak physics. The upgraded PCI is a complementary diagnostic to the DIII–D set of high-k measurements [6–8]. While the microwave scattering diagnostics provide single wavenumber measurements in three regions $k = 0 - 2$ cm^{-1}, $7 - 12$ cm^{-1}, $35 - 40$ cm^{-1}, the PCI provides continuous measurements over the wavenumber region $k = 2 - 30$ cm^{-1}. The work described in this article is focused towards a comparison between experiment and simulation of electron scale turbulence by describing a technique to add localization capability to the DIII–D Phase Contrast Imaging (PCI) diagnostic in the short wavelength (high-k) regime.

When initially developed, the DIII–D PCI measured density fluctuations in the outboard midplane region near the last closed flux surface (LCFS) [9]. The beam path was moved to the current Phase I geometry to cover the region $r/a > 0.7$ as shown in Fig. 1. Measurements were integrated along the beam chord and no spatial resolution was available. In these configurations, the PCI was responsible for making the first time-resolved measurements of correlation length and decorrelation time across the L-mode to H-mode transition [10, 11]. The differences between type I and type III ELMs were studied initially in DIII–D by the PCI system [12], and the time resolution was improved with wavelet analysis [13]. The PCI measurements suggesting zonal flows [14] were cited as early evidence for this phenomenon [15]. The PCI was the first diagnostic to measure the density fluctuation component of the Edge Harmonic Oscillation (EHO) coincident with the Quiescent H-mode (QH-mode) [16].

This article describes a new capability of the DIII–D PCI that takes advantage of the vertical variation of radial magnetic field to make localized measurements along the PCI chord. With this localization technique, the DIII–D PCI is now able to simultaneously measure density turbulence amplitude as a function of frequency,

expressed in terms of scattered and unscattered beams. The entire beam is sent through the plasma; the reference is the component of the beam unscattered by the fluctuating media while the signal beam is generated through the interaction of the incident laser and the fluctuating plasma. The unscattered reference beam is then phase shifted 90°. Finally, the signal and reference beams are combined through imaging optics and interfered on the detector. With this technique, variations in the index of refraction of the probed medium are then converted to intensity variations at the imaging plane. Figure 2 depicts the phase contrast technique.

To describe the PCI process mathematically, note that while the index of refraction of a magnetized plasma is generally anisotropic, for a tokamak plasma at infrared frequencies it is simply $N = (1 - \omega_{pe}^2/\omega^2)^{1/2} \simeq 1 - \omega_{pe}^2/2\omega^2$, where $\omega_{pe} = (n_e e^2/\epsilon_0 m_e)^{1/2}$ is the plasma frequency and ω is the frequency of the incident laser. Using the definition of the plasma frequency, the phase shift acquired by the incident laser can then be written [9, 18]

$$\tilde{\Phi}(\boldsymbol{x}_\perp, t) \simeq r_e \lambda_0 \int dz' n_e(\boldsymbol{x}', t), \qquad (1)$$

where λ_0 is the probe laser wavelength, r_e is the classical electron radius, n_e is the plasma electron density, and the integral is taken along the beam's direction of propagation. Because PCI measures the relative phase between the scattered and unscattered radiation, the absolute phase can be neglected and we can ignore the phase shift from propagation through the system and the background plasma density. The incident wavenumber (k_0) is chosen to produce far-forward scattering $(k_0 \gg k)$ where k is the wavenumber of plasma fluctuation. Integration along the PCI beam implies that the incident beam is only affected by plasma fluctuations that propagate nearly perpendicular to the incident beam. Taking this density fluctuation to be a single Fourier mode with wavenumber k in the plasma, the acquired phase shift can be expressed as $\tilde{\Phi} = \xi \cos(kx)$ where the x-direction is perpendicular to incident beam. The phase shift is small $(\xi \ll 1)$ and the resulting field in the plasma (object plane) can then be seen to consist of a sum of the reference and scattered components,

$$E_1^{\text{plasma}} = E_0 e^{i\tilde{\Phi}} \simeq E_0[1 + i\xi\cos(kx)]. \qquad (2)$$

The reference and scattered beams are focused with an off-axis parabolic mirror that spatially separates the scattered from the reference beam in the mirror's focal plane as shown in Fig. 2. The reference beam is then given an extra $\pi/2$ phase shift by centering it on the $\lambda/8$ deep groove of the *phase plate*; thus it traverses a longer path to acquire the prescribed phase shift. When interfered at the detector (image plane), the resulting field is then of
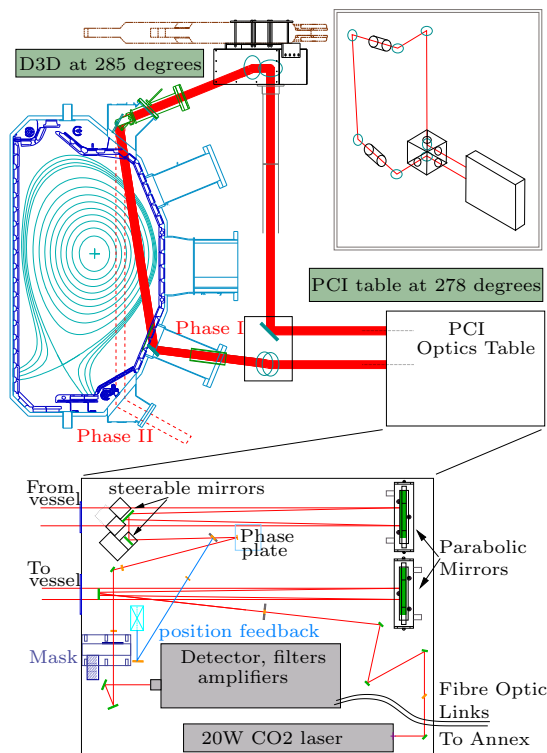

FIG. 1: (Color online), DIII-D PCI system overview with beam path in Phase I geometry (solid line) and future Phase II (dashed line) PCI chord geometry. Cylindrical focusing optics not shown for clarity. Upgraded amplifiers/filters condition the raw data and fibre optic links send data to the DIII-D Annex where it is digitized.

wavenumber, and plasma location. This level of detailed measurement will allow rigorous comparison with turbulence simulations.

The remaining parts of this article are arranged as follows: Section II provides an understanding of the PCI measurement and localization technique, Sec. III describes the PCI hardware and optical system, Sec. IV describes laboratory and plasma tests of the masking system, and finally Sec. V provides a summary.

II. DIAGNOSTIC PRINCIPLE

A. Phase Contrast Technique

Phase Contrast Imaging (PCI), first applied on the TCA Tokamak [17], is a form of internal reference beam interferometry that measures phase variations in the incident laser that are introduced by the probed medium. Unlike in traditional interferometry, the reference beam does not traverse a separate leg. In PCI, the incident laser is chosen of suitable wavelength so that the scattering is far forward or equivalently Raman-Nath. In such a small-angle scattering regime, if the phase object fluctuation is small then its effect on the incident beam can be

the form

$$E_2^{\text{detector}} = E_0[i + i\xi\cos(kx)], \qquad (3)$$

and the spatially varying component of the imaged intensity is then directly proportional to the original density variation in the plasma

$$I_2^{\text{detector}} \simeq E_0^2[1 + 2\xi\cos(kx)]. \qquad (4)$$

In practice, this intensity profile is sampled in space by a linear array of detector elements. The detector elements thus measure line integrated density fluctuations across the PCI chord; this data can be Fourier analyzed to provide spectral measurements of fluctuations propagating perpendicular to the viewing chord.

If the incident laser follows well governed Gaussian optics then the focus spot size and beam separation are (see Fig. 2)

$$\text{w}_0 = \frac{2f}{k_0\text{w}} \quad \text{and} \quad \Delta = \frac{kf}{k_0}, \qquad (5)$$

where f is the focal length of the parabolic mirror and w is the beam radius in the plasma. The phase plate groove width d is chosen to give an appropriate low-k cutoff, $k_{\min} = dk_0/2f$. This prevents low-k spectral pollution by wavenumbers that are unresolved due to the finite length of the detector array.
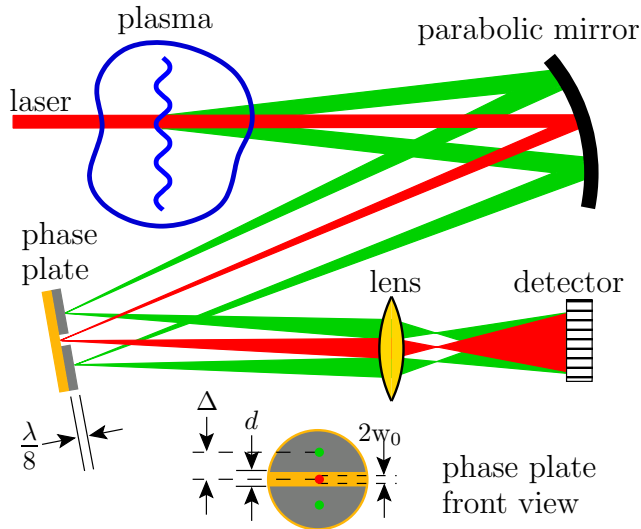

FIG. 2: (Color online), Schematic of PCI technique showing $\pi/2$ phase shift introduced by reflecting the unscattered beam off the *phase plate* groove. Distances and scattering angles not to scale.

B. Localization

When a scattering diagnostic is used to diagnose tokamak turbulence, we can exploit the magnetic geometry to gain localized measurements along the viewing chord [19]. This is possible because the component of the magnetic field perpendicular to the viewing chord varies as a function of chord height. As described in the previous section, PCI is only sensitive to fluctuations propagating perpendicular to the viewing chord. For electrostatic tokamak turbulence such as ITG and ETG modes, transport along field lines is large compared to cross-field transport. This means that locally $k_\perp \gg k_{||}$ and turbulent fluctuations propagate nearly perpendicular to the local magnetic field. These two constraints imply that PCI measures scattering from fluctuations that propagate perpendicular to both the viewing chord and the local magnetic field. Therefore, fluctuations from different plasma heights scatter at rotationally different angles about the PCI chord (see Fig. 3). This angle is a projection of the magnetic pitch angle onto a plane perpendicular to the PCI chord. This PCI chord-projected pitch angle (α) is then given by

$$\tan(\alpha) = \frac{B_\perp(z)}{B_\phi(z)}, \qquad (6)$$

where $B_\perp$ is the component of the poloidal magnetic field perpendicular to the PCI chord and B_ϕ is the toroidal magnetic field.

A component of the scattered radiation can be described in terms of the wavenumber k of the plasma mode and the height in the vessel z at which the scattering occurs. By combining Eq. 5 with Eq. 6, it can be seen that such a component is focused on the phase plate at a location $(\Delta(k), \alpha(z))$ in polar coordinates. This spatial separation of focal spots can be utilized by rotating a thin masking slit in the focal plane to selectively pass scattering events from a given height.

It is useful to introduce a Figure of Merit ($\mathcal{L}$) to estimate the effectiveness of a masking system for localized measurements. The minimum achievable resolution can be estimated by calculating the separation between points in the plasma that map to distinguishable points in the focal plane (*e.g.* are separated by at least the diameter of the focused beam spot). The pitch angle separating distinguishable points on the phase plate is simply $\delta\alpha = 2\text{w}_0/\Delta = 4/k\text{w}$ and thus

$$\mathcal{L} = \frac{dz}{d\alpha}\delta\alpha \simeq \frac{4B_\phi}{k\text{w}}\left(\frac{dB_\perp}{dz}\right)^{-1}, \qquad (7)$$

where z is the distance along the PCI chord, and we have assumed an optimal slit width and tokamak magnetic field geometry. It can immediately be seen that PCI localization improves for higher k fluctuations. For
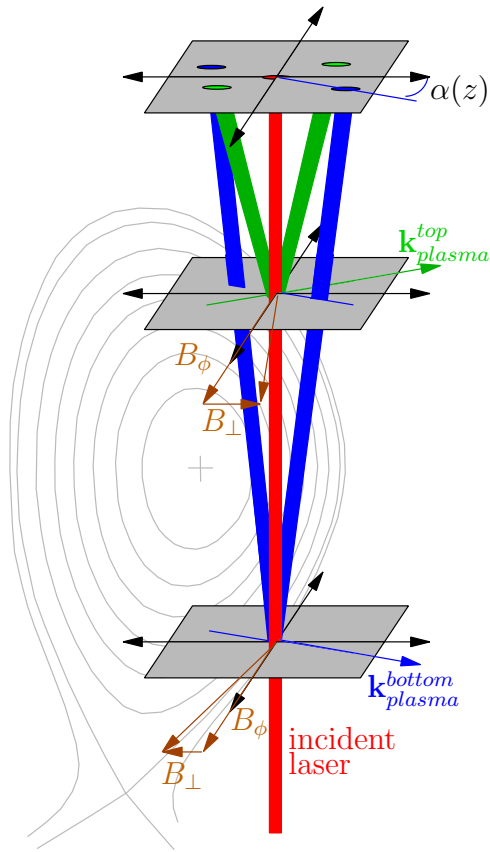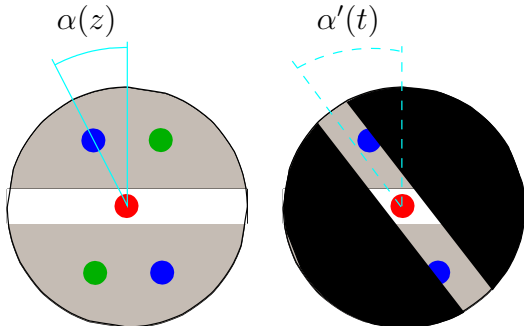
FIG. 3: Diagram of magnetic field pitch angle, associated plasma wavevector and scattered beams as a function of PCI chord height. Blue beams represent scattering from fluctuations at the bottom of the DIII-D PCI chord while green beams represent scattering from fluctuations at the top of the chord. Scattering angles not to scale.

a given plasma configuration, the only adjustment to the PCI that improves localization is to increase the size of the probe beam in the plasma. An optimum probe beam diameter can be determined for the desired high k cutoff given the various apertures in the optical path.

The figure of merit described above is a good approx-

imation of the localization capability of a PCI with a static masking slit. It is the plasma chord length-scale at which one can consider measurements separated by $\mathcal{L}$ (or equivalently $\delta\alpha$ in the focal plane) as independent. However, when the masking slit is rotated in time, a more rigorous analysis yields improved localization. A continuous spectrum as a function of mask angle can be related to the spectrum as a function of z as

$$S(z;k) \left| \frac{dz}{d\alpha} \right| = S(\alpha;k), \qquad (8)$$

$$\hat{S}(\alpha';k) = \int S(z;k) \left| \frac{dz}{d\alpha} \right| \mathcal{M}(\alpha' - \alpha;k)d\alpha, \qquad (9)$$

where $S(z;k)$ is the turbulence power per unit z in the plasma chord, $S(\alpha;k)$ is the turbulence power per unit pitch angle mapped to the focal plane, and $|dz/d\alpha|$ is the chord mapping density. In practice, the mapping density tends to peak at the plasma chord edges resulting in an artificial enhancement of edge turbulence. The mask response function $\mathcal{M}$ is the rotating mask transfer function. The plasma fluctuation power spectra measured at the detector array is given by $\hat{S}(\alpha';k)$, and α' is the mask slit angle. Note that the pitch angle α is limited in domain by tokamak magnetic geometry while α' represents the mask spin angle which is free to rotate through an entire revolution.

With this framework, it can be seen that interpretation of localized PCI measurements depends upon accurate knowledge of plasma magnetic geometry and the mask response function. The mask response $\mathcal{M}$ can be understood as the system response to a single plane wave mode in the plasma. In this formulation, it represents the actual response of the system, including all physical effects such as diffraction of the beam through the narrow mask slit. Details of the model and experimental verification of $\mathcal{M}$ will be discussed further in Sec. IV A, however the basic form is a peak at $\alpha = \alpha'$ falling to zero in both directions with a width proportional to $1/k$. Thus, the contribution from a small region in z is broadened out into a finite range in mask angle, limiting the resolution of the reconstruction. Equivalently, the convolution integral in Eq. 9 can be expressed as a multiplication in transform space, and thus the mask response function can also be thought of as a form of low-pass filter. The goal is then to deconvolve the measured spectra and map to plasma chord coordinates, yielding a localized measurement of turbulence power spectra. When interpreting these results, we must note that localized PCI measurements are not only spatially localized along the PCI chord but also in $\mathbf{k}$-space. This follows from the observation that the PCI measures fluctuations propagating perpendicular to the chord (e.g. $k_\perp$ has finite components in both k_r, k_θ at the plasma edge but $k_\perp = k_r$ where the chord is tangent to flux surfaces). It should

be noted that this localization technique assumes turbulence with correlation lengths that are small compared to the localized chord segment $\mathcal{L}$. In the range of wavenumbers of interest for high-k measurements, $L_C < 1$ cm and $\mathcal{L} > 5$ cm. This insures that fluctuation spectral power will add incoherently, which is a reasonable assumption for high-k driftwave turbulence. It should be noted that for longer wavelength fluctuations (where the localization technique is not used) L_C can become longer than 1 cm.

III. DIII–D EXPERIMENTAL SETUP

A. DIII–D Tokamak

DIII–D is a medium-size ($R = 1.66$ m, $a = 0.67$ m) diverted tokamak with a carbon first wall. Auxiliary heating is provided by neutral beams ($P_{inj} < 16$ MW), ICRF ($P_{source} < 6$ MW), and ECH ($P_{source} < 4$ MW) [20]. Typical ranges for plasma parameters are $B_0 = 1.5 - 2$ T, $I_p = 1 - 2$ MA, $\bar{n}_e = 1 - 5 \times 10^{19}$ m^{-3}, $T_{i0} = 2 - 10$ keV, $T_{e0} = 1 - 4$ keV. To estimate the regime of high-k ETG modes on DIII–D we take $T_e = 1$ keV, $L_n = L_{T_e} = a = 0.67$ m, $B_0 = 1.5$ T. Thus $v_{te} = 1.3 \times 10^7$ m/s and $\rho_e = 0.05$ mm. The strongest ETG growth is expected near $k_\perp \rho_e \sim 0.2$, which corresponds to roughly $k_\perp \sim 40$ cm^{-1} at $T_e = 1$ keV, though the parameters vary widely between different plasma discharges. Modeling predicts a frequency for ETG modes of $f \simeq 0.2(k_\perp \rho_e) v_{te}/(2\pi L_T)$ [5]. This is about 100 kHz near the peak growth, again assuming $L_T = a$. However, given that the high k spectrum peaks near the edge, L_T may be $0.1a$ or less, and the frequency would be 1 MHz even without Doppler shift.

B. PCI Hardware

The DIII–D PCI uses a 20 W, 10.6 μm CO_2 laser as its probe beam, see Fig. 1. The reflective phase plate consists of a ZnSe substrate with a gold reflective coating that has a groove of depth $\lambda/8$ cut through the plate diameter. The majority of the PCI system is located on an optics table in the machine hall. On this table, the PCI beam is expanded to a diameter of 5 cm and is collimated. It then leaves the optics table and is steered through the plasma by two in-vessel mirrors finally returning to the optics table for imaging, interference and detection. Noise is introduced into the PCI system by vibrations of these in-vessel and steering mirrors. Compensation for these vibrations is provided by using a feedback system comprised of two galvanometer-mounted steering mirrors, a quadrant position detector, and control circuitry. This feedback system has a bandwidth of approximately 1 kHz and maintains the focal spot position to an accuracy of 0.01 mm RMS. The rotating mask assembly, shown in Fig. 4, was designed and fabricated by Newmark Systems of Mission Viejo, CA and is mounted

on a 2 inch inner bore high speed bearing driven by a motor at speeds up to 3000 RPM. This results in up to 100 scans along the chord per second and the speed can be changed between shots from the DIII–D control room. The thin mask slit is cut into a removable plate which mounts to the rotation stage. This allows for slits of differing thicknesses (currently 0.5, 1.0, 2.0 mm) that provide flexibility in system magnification, beam size in the plasma, and mask placement.
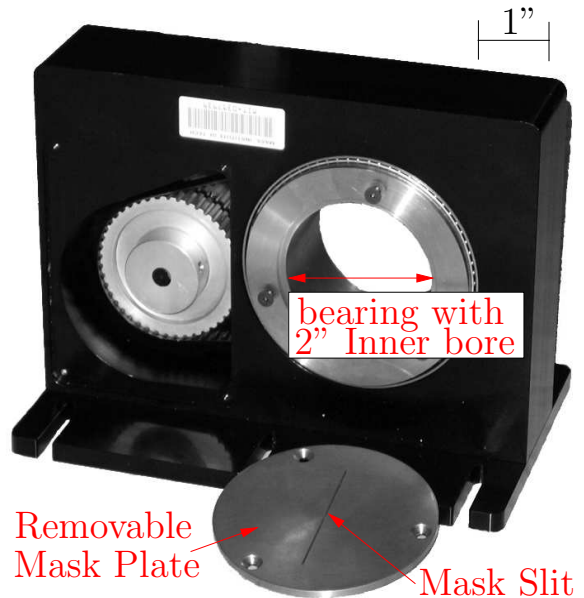

FIG. 4: (Color online), Rotating mask hardware assembly (removed from optics table for clarity). Removable mask plate has also been removed for clarity. The thin mask slit is cut into a removable plate so that the system can accommodate slits of different thickness.

The PCI uses a two lens imaging system that consists of 1.5 inch diameter plano-convex ZnSe optics. The optics must be large enough to accommodate the larger scattering angles of high-k fluctuations. The image system layout determines the overall magnification and thus the effective spacing of detector elements in the plasma. This provides the Nyquist wavenumber k_{max}, and is chosen to select the region in wavenumber space to diagnose. The PCI detector is a photovoltaic array of 16 HgMnTe elements with bandwidth greater than 10 MHz. The detector operates well within its saturation limits as the central uncoated strip of the phase plate acts as a partial reflector with a reflection coefficient of 17%. Additionally, the cylindrical lenses (described in more detail in Sec. III C) are only used for high-k measurements where the increased system magnification results in decreased laser intensity at the detector plane.

The current PCI chord is in the Phase I geometry as shown in Fig. 1. However, an upgrade is planned that

will move the chord into the Phase II geometry using the R-2 port, shown by the dashed line in Fig. 1. This will give the PCI access to $r/a \sim 0.4$ and thus the foot of the internal transport barrier (ITB). It has been suggested by recent theoretical work [21] that to observe pure ETG modes one should look in the shear stabilized ITG regimes, such as in ITBs where the nonlinearly upshifted ITG cascade modes would be stabilized by the strong E_r shear.

C.   Recent Upgrades

As previously described, the PCI localization improves with increasing wavenumber. Empirical data shows that PCI turbulence amplitude spectra falls as $1/k$. Therefore, it is necessary that the diagnostic have adequate signal-to-noise for the full time dependent analysis to improve resolution beyond that defined by Eq. 7. Although the PCI technique is inherently very sensitive (it is used to measure density perturbations from RF waves on Alcator C–Mod [22]), electron-scale fluctuations appear to be one to two orders of magnitude smaller in amplitude than the ion-scale counterparts. The DIII–D PCI has therefore received hardware upgrades over the past two years to improve system signal-to-noise ratio. New low noise amplifier/filter circuits were designed using modern components and fabrication techniques. These high-pass filters eliminate large amplitude, low frequency noise caused by mirror vibration. The PCI data transmission system, which sends output from the system detectors to digitizers located in the DIII-D annex, was upgraded using fibre optic links designed by Analog Modules of Longwood, FL. These links increase dynamic range to 55 dB over a bandwidth of 10 MHz. The system-wide noise floor is now at the thermal limit of the HgMnTe detectors.

To further improve system signal-to-noise ratio, cylindrical lenses are used in the imaging system to compress the beam along the axis perpendicular to the detector array, increasing signal intensity by a factor of 2 to 5 without affecting the imaging properties. This signal enhancing optical setup requires dual cylindrical lenses to break the imaging into independent orthogonal systems parallel and perpendicular to the detector array. Both axes must have image planes coincident with the detector array. This setup can be configured with a cylindrical lens focusing along each axis or with both cylindrical lenses focusing along the same axis. By using the configuration with both lenses focusing along the same axis, the lenses may be removed without the need to re-adjust the rest of the system optics to return to a traditional imaging configuration.

D.   Mapping

An understanding of the chord mapping is needed to translate between scattered pitch angle and plasma location, to calculate $|dz/d\alpha|$, and to represent the PCI measured wavevector (perpendicular to the chord) in terms of the more physically relevant (k_r, k_θ) components. The mapping from PCI chord height to scattering pitch angle, $\alpha(z)$, depends on the specific magnetic geometry and is not always a monotonic function. Non-monotonic mappings are more pronounced as the PCI chord passes closer to the plasma core.

Figure 5a shows PCI chord mappings for two PCI chord locations in a lower single null L-mode plasma with $q_{95} = 5.5$. Here, q_{95} is the tokamak safety factor evaluated at the 95% flux surface. Currently in use is the PCI Phase I geometry, which is restricted to the outer plasma region while the planned Phase II geometry reaches the plasma interior (see Fig. 5c).
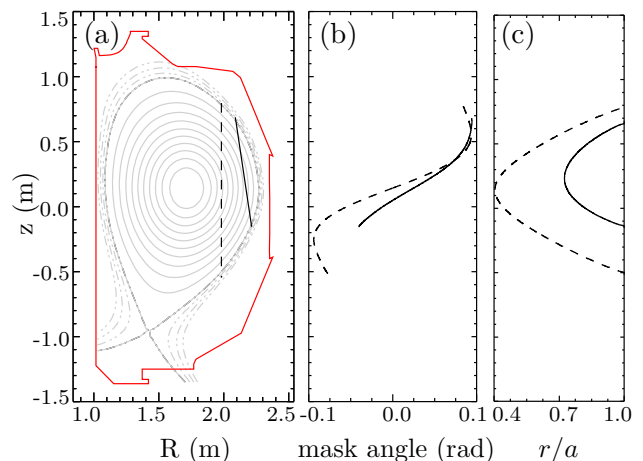

FIG. 5: (Color online), PCI chord mapping for both Phase I (solid line) and Phase II (dashed line) geometries during L-mode lower single null (LSN) discharge with $q_{95} = 5.5$. (a) Flux surfaces and chord locations. (b) Mask pitch angle as a function of chord height shows non-monotonic mapping for Phase II geometry but monotonic mapping for Phase I geometry. (c) Chord plasma location shows Phase I geometry $r/a > 0.7$ and Phase II geometry $r/a > 0.4$.

From the mappings shown in Fig. 5b, it is clear that the Phase II geometry suffers from non-monotonic mappings near the chord edges. This feature is worse for large q_{95} where the poloidal field becomes relatively weak due to peaked current profiles. However, even at $q_{95} = 5.5$, the mapping in the inner region of the PCI chord $0.4 < r/a < 0.55$ is single valued and the localization technique will be particularly useful in isolating turbulence from the shear regions of the ITB.

In the current Phase I geometry, the mapping is generally well behaved for the lower portion of the PCI chord while the upper portion of the chord ($z > 0.3$) can become difficult to resolve and even non-monotonic (see Fig. 6a). The best localization will be achieved where
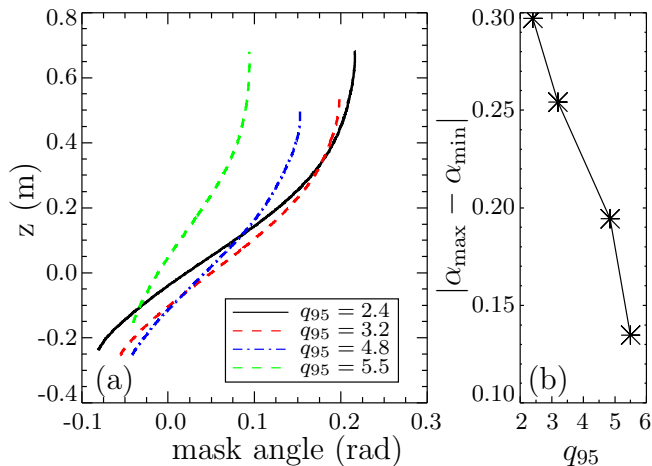
FIG. 6: (Color online), (a) PCI chord mapping of Phase I geometry for four different discharge geometries with increasing values of q_{95}. (b) Scaling of pitch angle full range shows better localization for low q_{95}.

the PCI chord is tangent to flux surfaces and thus at the closest approach to the plasma core. As can be seen in Fig. 6b, the ability to localize fluctuations is better for lower q_{95}, due to fluctuations being spread over a larger range in scattered pitch angle in the focal plane. Here we define $\Delta\alpha$ as the full range of scattered pitch angle,

$$\Delta\alpha = \alpha_{max} - \alpha_{min}. \qquad (10)$$

In the current geometry, the upper edge of the PCI chord suffers from large chord mapping density per unit mask pitch angle $|dz/d\alpha|$ for many magnetic geometries. This feature is one reason the proper analysis based on Eq. 9 is essential to determining the spatial variation in the turbulence from the PCI data. Care is thus needed when interpreting localized spectral measurements, as will be discussed further in Sec. IV B.

E. Mask Focal Plane

Conceptually, the mask is imagined as coincident with the surface of the phase plate. Practically, this cannot be realized because the mask must be slightly separated from the phase plate to allow rotation. This small offset would cause the mask to block all radiation because of the narrowness of the slit and the angle of reflection off the phase plate. However, any optical system obeying geometric optics has multiple focal planes (i.e. locations where a perfectly collimated PCI laser would form a waist). The mask is placed at one of the secondary focal planes which is optically equivalent to placement at the phase plate focal plane. The placement, shown in Fig. 7, permits proper operation of the mask and also provides an arbitrary magnification, allowing the beam focus spot size to be optimized for a given mask slit width.

Placing the mask very close to the phase plate may be

possible on systems that use a transmissive phase plate [23], but this is probably not practical on a tokamak PCI due to the small range in scattered pitch angle (see Eq. 6) and hence tight tolerances.

A similar localization technique is currently in use on the LHD heliotron, which has a poloidal field much larger than that in a tokamak. Rather than a mask, they use a 2-D detector to record the data and then fit the data to estimate $S(z,k)$ [24]. While LHD has a scattering pitch angle full range $\Delta\alpha \sim 80°$, this adaptation can operate in a region of smaller $\Delta\alpha$ using asymmetric magnification (the so-called "zoom" mode technique [24]) making it potentially tractable for a tokamak device. However, the spatial resolution and wavenumber resolution are directly related to the number of detector channels. For a tokamak with much smaller $\Delta\alpha$ (typically 12°), the rotating mask technique has the potential to achieve greater spatial resolution at high wavenumber with more modest detector and digitizer requirements.
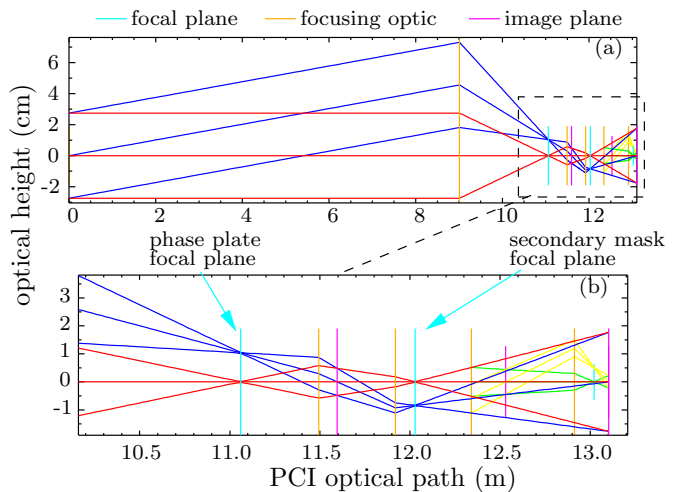

FIG. 7: PCI optical layout showing unscattered (red) and one $k = 30$ cm^{-1} scattered (blue) beam composed of rays along the center-line of the beam and the $1/e$ electric field radii. (a) Full PCI optical path from plasma (object) to detector (image). (b) Imaging optics showing creation of secondary focal plane for rotating mask placement.

IV. TESTS AND CHARACTERIZATION

A. Laboratory Tests

As described in Sec. II B, the ability to properly interpret localized measurements made by a rotating mask system requires accurate knowledge of the mask response function $\mathcal{M}$ in Eq. 9. The mask response function is defined as the system response to a single plane wave mode in the plasma. This response is dependent on the focused beam structure (e.g. presence of higher order modes), the mask slit width, and the diffraction of both the scattered and unscattered beams through the mask slit.

The model used for computing $\mathcal{M}$ consists of the following assumptions: Gaussian electric field profiles incident on the mask plate for both the scattered and unscattered beams, the mask acts to zero the electric field where the incident beam profile is blocked by the mask plate, and that the mask plate is infinitely thin and the unblocked portion of the beam is not affected. With this as a starting point, the electric field profile of the incident scattered beam can be written in the form $E_s = E_s(\mathbf{x}; \mathrm{w}_0, \Delta(k), \alpha(z))$ and the unscattered beam $E_0 = E_0(\mathbf{x}; \mathrm{w}_0)$ where $\Delta(k)$, w_0, and $\alpha(z)$ are previously defined in Eqs. 5 and 6. We introduce the clipping function $K = K(\mathbf{x}; \alpha', l)$ where α' is the mask plate angle (see Fig. 3) and l is the mask slit width. The value of the function K is unity over the region of the mask slit where the beam is not blocked and $K = 0$ where the beam is blocked by the mask plate.

Ignoring diffraction effects, the mask function is then simply the fraction of focused beam power passing through the rotating slit, $\mathcal{M}(\alpha' - \alpha; k) = \int d^2x \; E_s^2 K / \int d^2x \; E_s^2$. While useful for understanding scalings with mask slit width and wavenumber, ignoring diffraction is insufficient to properly characterize measurements of the mask response function because this effect tends to spread out the beam at the detector plane in the direction perpendicular to the mask slit.

To include diffraction effects, the scattered and unscattered beams are propagated from the mask focal plane to the detector plane using scalar diffraction theory [25]. We define a scalar diffraction operator $\hat{\mathcal{D}}$ as

$$E_{\mathrm{det}}(\mathbf{x}) = \hat{\mathcal{D}}(E_{\mathrm{mask}}(\mathbf{x}')) =$$

$$\frac{k}{2\pi i} \int d^2x' \; \frac{e^{ikR}}{R} \left(1 + \frac{i}{kR}\right) \frac{\mathbf{n}' \cdot \mathbf{R}}{R} \; E_{\mathrm{mask}}(\mathbf{x}'), \quad (11)$$

where $\mathbf{x}'$ are coordinates in the mask focal plane, $\mathbf{x}$ are coordinates in the detector plane, $\mathbf{R} = \mathbf{x} - \mathbf{x}'$, $R = |\mathbf{R}|$, $\mathbf{n}'$ points along the beam direction of propagation, and the integral is performed over the mask focal plane. Thus the total electric field at the detector plane is the interference of the propagated scattered and unscattered beam electric fields $E_{\mathrm{det}}^K = \hat{\mathcal{D}}(E_s K) + \hat{\mathcal{D}}(E_0 K)$. The resulting field in the detector plane has a sinusoidal intensity profile with amplitude A_K. We perform the same computation without the presence of the mask ($K = 1$) to obtain the total field at the detector $E_{\mathrm{det}}^1 = \hat{\mathcal{D}}(E_s) + \hat{\mathcal{D}}(E_0)$ with intensity amplitude A_1. The mask response function is then simply the ratio $\mathcal{M}(\alpha' - \alpha; k) = A_K / A_1$.

Measurements of the mask response were obtained by using an ultrasonic loudspeaker provided by Ultra Sound Advice, U.K. Originally developed for bat research, this loudspeaker is a broadband cw ultrasound device capable of 85 dB sound pressure level (SPL) from 30 kHz to greater than 150 kHz. Using ultrasound in air at these frequencies allows the launching of single wavenumber modes from $6 - 40$ cm^{-1}. If the 5 cm loudspeaker membrane is placed within 3 cm of the PCI laser beam, then the sound wavefront radius of curvature is large and the wavefronts are sufficiently planar to use for mask response function measurements. These data were obtained over a range in wavenumbers from $6 - 27$ cm^{-1}.
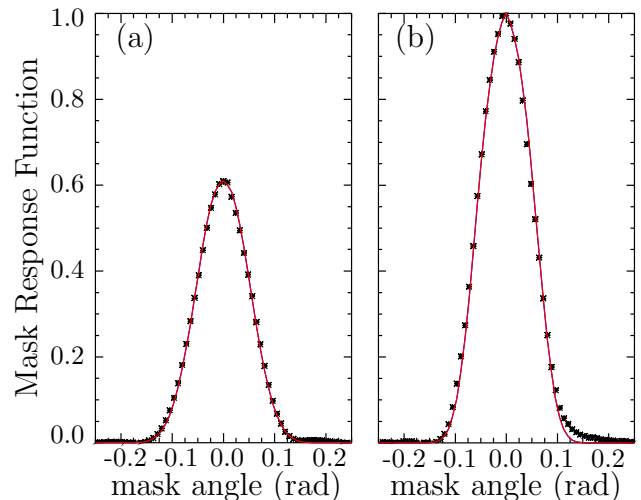

FIG. 8: (Color online), Measurements of the mask response function using (a) 0.5 mm slit at $k = 14$ cm^{-1} and (b) 1.0 mm slit at $k = 20$ cm^{-1} show good agreement between the scalar diffraction model (solid line) and measurements with the cw ultrasound loudspeaker (symbols). (a) shows that the peak response for the 0.5 mm slit is 60% of the system response without the mask slit.

The scalar diffraction model agrees well with measurements of the mask response structure as shown in Fig. 8 where the symbols are the measured mask response function using the cw ultrasound loudspeaker and the solid line is the calculated response using the scalar diffraction model. While the calculated response scale is absolute, the data is fit using an arbitrary amplitude factor to account for the variations in response of the cw loudspeaker. The peak response of the 0.5 mm mask slit is $\sim 60\%$ of that of the 1.0 mm slit because the laser focal spot size (w_0) at the mask plane has a $1/e$ electric field radius of 0.28 mm. Thus, even when the response is maximum ($\alpha = \alpha'$), the smaller 0.5 mm mask slit provides substantial clipping and diffraction that results in a lower system signal-to-noise ratio.

Figure 9 plots the measured and modeled full width at half maximum (FWHM) of the mask response function vs. wavenumber for 3 different mask slit widths (2.0 mm, 1.0 mm, 0.5 mm). As expected, the measured widths for each wavenumber scale as $1/k$. Solid lines are the calculated FWHM from the scalar diffraction model. Agreement is good with a relative error generally less than 5%. At higher frequencies, the loudspeaker membrane appears to vibrate in modes other than the fundamental making mask response measurements at high k difficult. The 2.0 mm mask slit provides poor resolution due to its broad response shown by the large FWHM

measurements. While the 0.5 mm mask slit has the narrowest FWHM and therefore the best resolution, it causes an undesirable amount of diffraction and signal-to-noise is degraded as previously described. The 1.0 mm mask slit is generally used as it provides a good compromise between resolution and signal-to-noise.
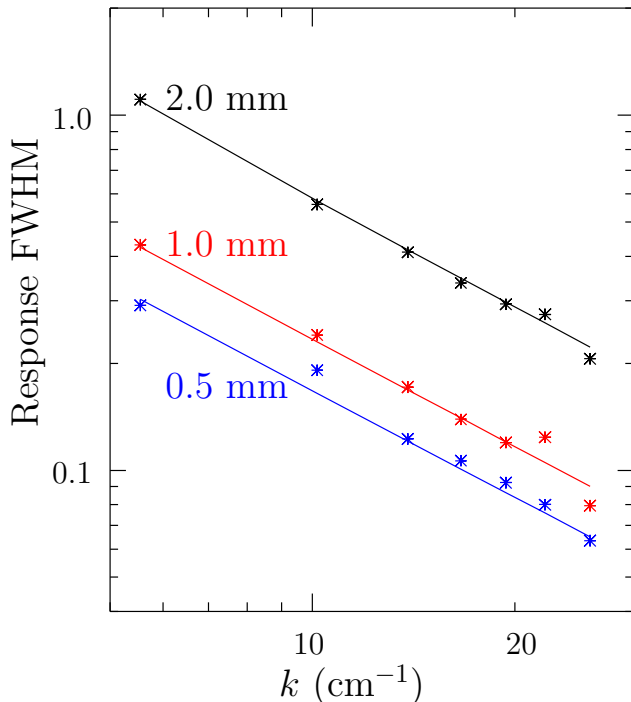

FIG. 9: (Color online), FWHM of mask response function over PCI wavenumber range shows good agreement for all mask slit widths. Measurements using cw ultrasound loudspeaker shown as symbols and scalar diffraction model shown as solid lines.

B.   Plasma Tests

While calibration data can be collected under ideal conditions, plasma turbulence measurements have the contradictory requirements of long time averaging for improved signal-to-noise and short time averaging for responsiveness to changing plasma conditions. The rotating mask analysis technique thus requires a balancing of integration times to yield quality localized measurements. The practical rate at which localized measurements can be recorded is less than the hardware limitation of 100 profiles/sec and is set by system noise, the desired spatial resolution and the desired frequency resolution.

The analysis procedure consists of computing power spectra every $2/\delta f$ seconds where δf is the desired frequency resolution. These power spectra are then averaged over multiple realizations, typically $2 < N < 16$. Sampling in the mask angle domain is therefore $\alpha_{i+1} - \alpha_i = 2\pi N F/\delta f$ where F is the mask rotation

rate in profiles/sec. This sets the grid on which Eq. 9 is inverted, and ultimately the maximum spatial resolution $\Delta z = z(\alpha_{i+1}) - z(\alpha_i)$. Further averaging can be performed over multiple mask profiles provided the plasma conditions remain stationary. The parameters δf and F are varied to optimize the analysis for each experiment so better spatial and frequency resolution are produced for plasmas with long steady-state periods.

Measurements during various plasma conditions have been made with the new rotating mask system. Plasma data have been obtained that show $S/N > 1$ for $k \lesssim 25$ cm^{-1} and calibrations using ultrasonic waves have confirmed proper operation of the PCI to at least $k = 37$ cm^{-1}. While system signal-to-noise is the current limiting factor in spatial resolution of the localization technique, the DIII–D PCI shows unmistakable structure in the measured spectrum as a function of mask angle. The following data are presented to best illustrate the analysis procedure of this localization technique.
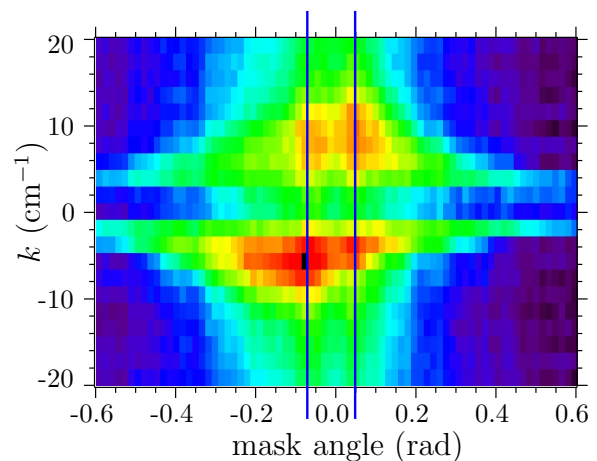

FIG. 10: Measured spectrum of plasma turbulence (raw data before the inversion removes instrumental response) by the rotating mask system, integrated over frequency range $150-300$ kHz. Vertical blue lines represent mapping of LCFS locations in pitch angle space. By convention, $+k$ is defined as modes propagating approximately radially outward ($+\hat{R}$), and $-k$ is defined as modes propagating approximately radially inward ($-\hat{R}$). Colors in log scale.

Figure 10 plots a measured fluctuation power spectrum ($\hat{S}(\alpha'; k)$ as in Eq. 9) during ECH heating of an L-mode discharge showing PCI signal integrated from $150 - 300$ kHz, and $S/N > 1$ for $k \lesssim 20$ cm^{-1}. The vertical lines represent the edges of the plasma. Two distinct features are immediately apparent: 1) The mask response does indeed get more narrow as k increases, and 2) turbulence is highly asymmetric with respect to inward/outward propagation. The measured power spectrum extends beyond the LCFS (shown by vertical lines in Fig. 10) due to the finite width of the mask response function. Recall that PCI measures wavevectors perpendicular to the viewing chord and that the PCI beam is nearly vertical ($+\hat{z}$ direction); by convention we define positive k as approxi-

mately radially outward $(+\hat{R})$ and negative k as radially inward $(-\hat{R})$. Inward propagating modes are particularly strong at the bottom of the PCI chord (negative mask angle edge). These features were verified by rotating the mask in the opposite direction during a repeat shot, thus instead of sweeping through the plasma from bottom to top of the PCI chord, the localized volume sweeps from top to bottom; the measured fluctuation power as a function of time reversed as expected.

The DIII–D PCI has previously measured turbulence amplitude spectra to scale as $1/k$. Since the localization becomes better at high k, analysis of the rotating mask data is limited by low signal-to-noise at high k. Currently, analysis is being performed by choosing a parametrized trial function for $S(z;k)$ and varying the parameters to minimize the error between $\hat{S}(\alpha';k)$ calculated from the trial function (via Eq. 9) and the observed $\hat{S}(\alpha';k)$. This process is necessary because the inversion of Eq. 9 is ill-conditioned; the spectral structure of $\mathcal{M}$ will lead to erroneous noise amplification even under a Weiner LTI filtering approach [26]. The trial function $S(z;k)$ used in the initial analysis is chosen to be a sum of N Gaussians uniformly spaced in α (i.e. $\alpha_i = \alpha_{\min} + i\delta\alpha$ where $\delta\alpha = \frac{\alpha_{\max}-\alpha_{\min}}{N-1}$ and $i = 0...N-1$). The gaussian widths scale to be smaller as more gaussians are introduced (by increasing N), allowing the widths to scale proportional to the width of the mask response function $\mathcal{M}(\alpha'-\alpha;k)$. The gaussians located at $i = 0$ and $i = N-1$ are "clipped" such that no fluctuation power is allow beyond the mapping extrema $\alpha_{\min}$ and $\alpha_{\max}$. Each gaussian's amplitude β_i is a parameter used in the fitting process. Therefore, the parameterized trial function can be written

$$S(z;k) = \sum_{i=0}^{N-1} \beta_i e^{-\left(\frac{\alpha(z)-\alpha_i}{\delta\alpha/2}\right)^2} \qquad (12)$$

valid from $\alpha_{\min} \leq \alpha(z) \leq \alpha_{\max}$ and $S(z;k) = 0$ everywhere else. This trial function is continuous over the valid domain in α-space and has structure characteristic of the width of the mask response function. Figure 11 shows that $\hat{S}(\alpha';k)$ reconstructed from the trial function accurately reproduces the observed $\hat{S}(\alpha';k)$.

Examples of the turbulence power spectrum $S(z;k)$ calculated using this technique are shown in Fig. 12. It is clear that the peaking of power spectra at the mapping extrema $(\alpha_{\min}, \alpha_{\max})$ is not solely due to peaking in the chord mapping density, $|dz/d\alpha|$. Figure 12 shows PCI turbulence power for $k = \pm 9.6$ cm^{-1} with and without ECH heating from the same discharge as Fig. 10. In both heating regimes, turbulence peaks at the plasma chord edges. ECH heating increases the outward propagating modes at both edges while marginally altering the inward propagating turbulence modes.
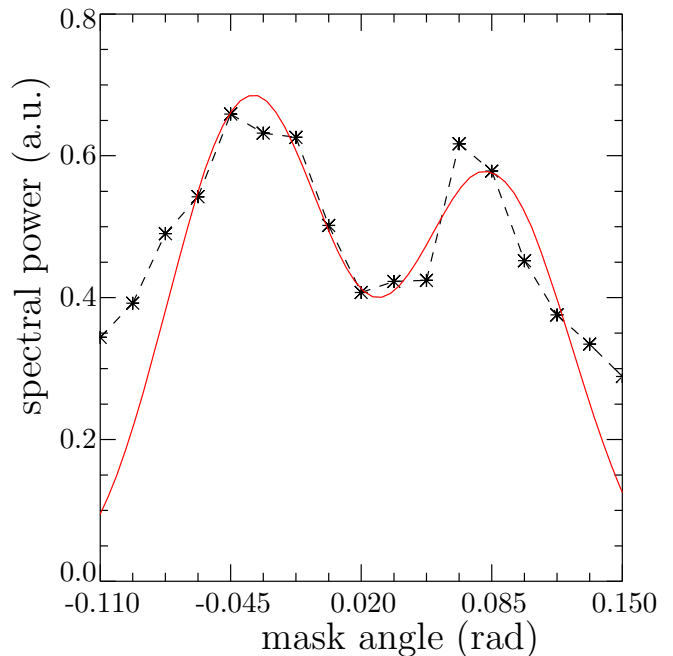

FIG. 11: (Color online), Observed $\hat{S}(\alpha';k)$ (dashed line with symbols) is a single slice of Fig. 10 at $k = -13.5$ cm^{-1} (raw data before inversion analysis). The reconstructed $\hat{S}(\alpha';k)$ (solid line) is the best fit of the prototyped $S(z;k)$ convolved with the mask response function.

V. SUMMARY

Modifications to the DIII–D Phase Contrast Imaging diagnostic have been designed and implemented to make the first spatially localized PCI measurements of a tokamak plasma. The difficulties in applying this technique to the small B_θ/B_ϕ plasmas in a tokamak required a novel version of the pitch angle masking technique. Calibrations show operation of the system to be very close to the theoretical expectations.

Spatial localization is improved at higher wavenumbers, and this is part of a general program to operate the DIII–D PCI diagnostic with the goal of measuring plasma fluctuations with wavenumbers up to 40 cm^{-1}. Initial results show that the PCI can provide localized measurements with $S/N > 1$ for $k \lesssim 25$ cm^{-1}; the example shown provides an instance of turbulence near 10 cm^{-1} peaking at the plasma edge.

Calibrations using ultrasonic waves in air confirm that this new capability provides measurements in the range $2 < k < 30$ cm^{-1}, 10 kHz $< f < 10$ MHz, and analysis of magnetic field mappings generally result in a radial range of $0.7 < r/a < 1$. Localized PCI measurements will be a valuable tool for measuring short wavelength turbulence in order to understand electron scale heat transport as well as testing the validity of various theoretical models of turbulent transport.

The implementation of PCI as a turbulence diagnostic is comparatively simple. The requirements for in-vessel
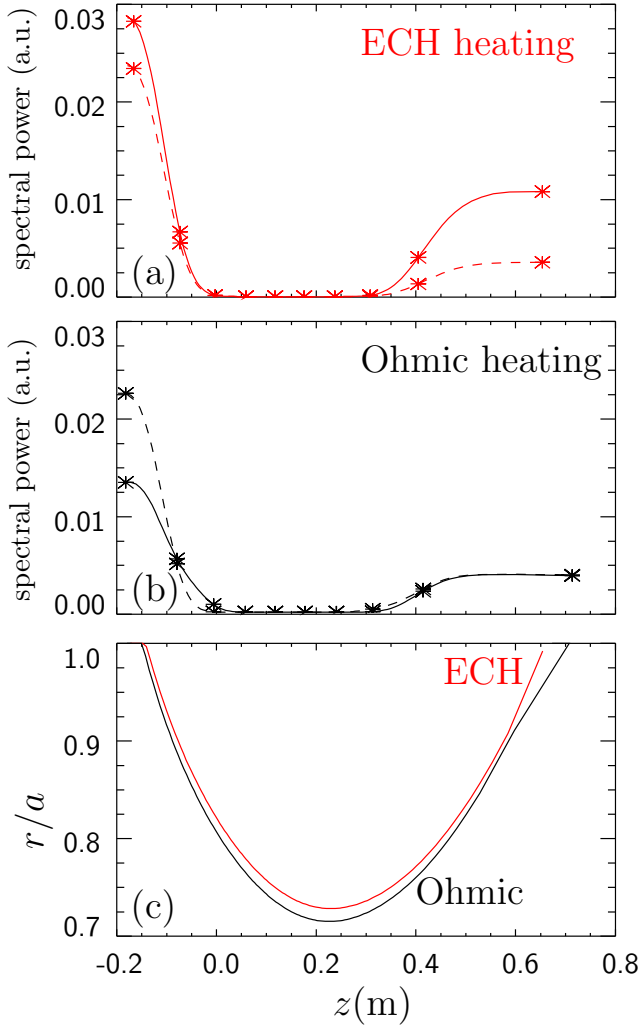
FIG. 12: (Color online), Turbulence spectra $S(z;k)$ calculated for $k = -9.6$ cm^{-1} (dashed line) and $k = +9.6$ cm^{-1} (solid line) during (a) ECH heating and (b) Ohmic heating of a L-mode discharge. Turbulence is dominated by the plasma edge and increases in the outward propagating direction during the application of ECH heating. (c) Plasma radial location of PCI chord during both heating regimes.

equipment are minimal, it operates over a wide range of plasma parameters, it provides continuous measurements over a range of wavenumbers, and the diagnostic is completely non-perturbative. These factors make PCI ideal for measuring turbulence in future reactor-relevant machines.

[1] B. A. Carreras, IEEE Trans. Plasma Sci. **25** (1997).
[2] A. M. Dimits, G. Bateman, M. A. Beer, B. I. Cohen, W. Dorland, G. W. Hammett, C. Kim, J. E. Kinsey, M. Kotchenreuther, A. H. Kritz, L. L. Lao, J. Mandrekas, W. M. Nevins, S. E. Parker, A. J. Redd, D. E. Shumaker, R. Sydora, and J. Weiland, Phys. Plasmas **7**, 969 (2000).
[3] M. Kotschenreuther, W. Dorland, G. W. Hammett, and M. A. Beer, Phys. Plasmas **2**, 2381 (1995).
[4] F. Jenko, W. Dorland, M. Kotschenreuther, and B. N. Rogers, Phys. Plasmas **7**, 1904 (2000).
[5] W. M. Nevins, J. Candy, S. Cowley, T. Dannert, A. Dimits, W. Dorland, C. Estrada-Mila, G. W. Hammett, F. Jenko, K. J. Pueschel, and D. E. Shumaker, Phys. Plasmas **13**, 122306 (2006).
[6] T. L. Rhodes, W. A. Peebles, J. C. DeBoo, R. Prater, J. E. Kinsey, G. M. Staebler, J. Candy, M. E. Austin, R. V. Bravenec, K. H. Burrell, J. S. deGrassie, E. J. Doyle, P. Gohil, C. M. Greenfield, R. J. Groebner, J. Lohr, M. A. Makowski, X. V. Nguyen, C. C. Petty, W. M. Solomon, H. E. St. John, M. A. VanZeeland, G. Wang, and L. Zeng, Plasma Phys. Control. Fusion **49**, B183 (2007).
[7] T. L. Rhodes, W. A. Peebles, M. A. VanZeeland, J. S. deGrassie, G. R. McKee, G. M. Staebler, J. C. DeBoo, E. J. Doyle, M. Gilmore, P. Gohil, C. M. Greenfield, R. J. Groebner, X. V. Nguyen, G. Wang, and L. Zeng, Nucl. Fusion **47**, 936 (2007).
[8] T. L. Rhodes, W. A. Peebles, X. Nguyen, M. A. VanZee-

land, J. S. deGrassie, E. J. Doyle, G. Wang, and L. Zeng, Rev. Sci. Instrum. **77**, 10E922 (2006).

[9] S. Coda, M. Porkolab, and T. N. Carlstrom, Rev. Sci. Instrum. **63**, 4974 (1992).

[10] S. C. Coda, M. Porkolab, and K. H. Burrell, Phys. Letters A **273**, 125 (2000).

[11] S. Coda, M. Porkolab, and K. H. Burrell, in *Proc. of 22nd European Conf. on Controlled Fusion and Plasma Physics, Bournemouth*, volume 19C, part 1, pages I–297, European Physical Society, 1995.

[12] S. Coda, M. Porkolab, and K. H. Burrell, Nucl. Fusion **41**, 1885 (2001).

[13] J. C. Rost, M. Porkolab, B. J. Youngblood, G. R. McKee, T. L. Rhodes, R. A. Moyer, and K. H. Burrell, Bull. Am. Phys. Soc. **46**, 220 (2001).

[14] S. Coda, M. Porkolab, and K. Burrell, Phys. Rev. Lett. **86**, 4835 (2001).

[15] P. H. Diamond, M. N. Rosenbluth, F. L. Hinton, M. Malkov, J. Fleischer, and A. Smolyakov, in *Proceedings of the 17th IAEA Fusion Energy Conference, Yokohama, Japan*, 1998, IAEA-CN-69/TH3/1.

[16] K. H. Burrell, M. E. Austin, D. P. Brennan, J. C. D. an dE. J. Doyle, C. Fenzi, C. Fuchs, P. Gohil, C. M. Greenfield, R. J. Groebner, L. L. Lao, T. C. Luce, M. A. Makowski, G. R. McKee, R. A. Moyer, C. C. Petty, M. Porkolab, C. L. Rettig, T. L. Rhodes, J. C. Rost, B. W. Stallard, E. J. Strait, E. J. Synakowski, M. R.

Wade, J. G. Watkins, and W. P. West, Phys. Plasmas **8**, 2153 (2001).

[17] H. Weisen, Plasma Phys. Control. Fusion **28**, 1147 (1986).

[18] M. Porkolab, J. C. Rost, N. Basse, J. R. Dorris, E. Edlund, L. Lin, Y. Lin, and S. Wukitch, IEEE Trans. Plasma Sci. **34**, 229 (2006).

[19] A. Truc, A. Qumneur, P. Hennequin, D. Grsillon, F. Gervais, C. Laviron, J. Olivain, S. K. Saha, and P. Devynck, Rev. Sci. Instrum. **63**, 3716 (1992).

[20] J. L. Luxon, Nucl. Fusion **42**, 614 (2002).

[21] R. Waltz, J. Candy, F. Hinton, C. Estrada-Mila, and J. Kinsey, Nucl. Fusion **48**, 741 (2005).

[22] E. Nelson-Melby, M. Porkolab, P. T. Bonoli, Y. Lin, A. Mazurenko, and S. J. Wukitch, Phys. Rev. Lett. **90**, 155004 (2003).

[23] S. Kado, T. Irie, K. Muraoka, K. Matsuo, K. Tanaka, K. Kondo, F. Sano, and T. Obiki, Jpn. J. Appl. Phys. **34**, 6492 (1995).

[24] C. A. Michael, K. Tanaka, L. Vyacheslavov, A. Sanin, K. Kawahata, and S. Okajima, Rev. Sci. Instrum. **77**, 10E923 (2006).

[25] C. J. Bouwkamp, Rep. Prog. Phys. **17**, 35 (1954).

[26] R. Neelamani, H. Choi, and R. Baraniuk, IEEE Trans. Signal Proc. **52**, 418 (2004).